

Assessment of sub-micron subsurface damage in glass

JING XU,¹ GONG CHEN,² JIE QIAO,² AND JOHN C. LAMBROPOULOS^{1,*}

¹University of Rochester, Department of Mechanical Engineering, 500 Joseph C. Wilson Blvd., Rochester, NY 14627

²Rochester Institute of Technology, Chester F. Carlson Center for Imaging Science, One Lomb Memorial Drive, Rochester, NY 14623

*john.lambropoulos@rochester.edu

Abstract: We present a new experimental method for assessing sub-micron level subsurface damage (SSD) on optical glass. The method correlates surface characteristics such as fracture toughness and Young's modulus via nanoindentation with penetration depth into the tested surfaces, at different overall penetration depths as revealed by magnetorheological finishing (MRF) spotting techniques. Our results on ground surfaces suggest that low surface roughness does not necessarily imply the absence of SSD. We also compared SSD on surfaces processed by deterministic microgrinding and femtosecond (fs) laser polishing. The fs-laser polished surfaces revealed no detectable SSD, thus establishing the feasibility of fs-laser polishing for precision optical manufacturing.

1. Introduction

Subsurface damage (SSD) at optical surfaces refers to the damage that is under the surface roughness and is invisible from the surface. Components of subsurface damage include median (propagating downwardly in the loading direction) and lateral (extending upwardly in parallel to the surface) cracks, dislocations, residual stresses, etc. [1] Figure 1 shows schematically the subsurface damage structure in optical glass in a cross-sectional view.



Fig. 1. Schematic illustration of subsurface damage. On the top is surface roughness (SR) left by manufacturing process. Beneath it are microcracks that may induce residual stress.

Subsurface damage is in almost all cases unwanted in finished surfaces because it can be the source of component responsible for low mechanical or optical performance. The median and lateral cracks may grow during cyclic loads and finally cause fatigue failure. The residual stress within the subsurface damage layer leads to Twyman effect [2]. For an optical material, SSD can also lead to scattered light that reduces image contrast and catastrophic fracture, especially in high power lasers. Therefore, it is crucial to precisely determine SSD and possibly reduce or mitigate it by a finishing process. Developed approaches for evaluating SSD include destructive (also known as invasive) and non-destructive ones [1].

Destructive evaluation places permanent changes to the tested surface, usually by removing material mechanically and/or chemically. Typical destructive methods include taper-sectioning technique [3,4], combined sectioning (cross-sections/bonded interface) technique, and chemical etching methods [5-7]. These methods can be combined for better accuracy and ease of implication [8]. The main idea of destructive methods is to evaluate SSD through the evolution of surface roughness and/or morphology, typically measured by interferometer or scanning electron microscopy (SEM), with material removed. Destructive methods are usually precise for SSD depths starting from microns.

For the taper-sectioning method, magnetorheological finishing (MRF) spots have been widely used to create tapers because of its advantages over traditional polishing in terms of

controllability and newly-induced subsurface damage [9,10]. The magnetorheological (MR) fluid contains carbonyl iron (CI) particles coated by abrasive particles, usually nano-sized diamonds, or ceria particles. The CI particles ensure that the fluid can be constrained into a ribbon by the magnetic field on the wheel, and the abrasives are responsible for the shear stress on the surface with materials being removed, as shown in Fig. 2. It is less aggressive and thus does not induce any new damage [11].

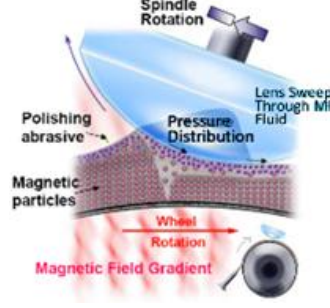


Fig.2. Schematic of the MRF contact zone. Figure adapted with permission from J. Nelson et al. (2003) [12].

Non-destructive evaluation methods do not cause any changes to the tested surface and evaluate SSD mainly through the correlation of damaged material with Raman shift/Raman intensity ratio [13] and Bragg-peak width in X-ray diffraction [14].

Another frequently reported non-destructive method is to find the correlation between the surface roughness (SR) with the depth of the subsurface damage. This correlation usually varies with materials and machining processes. It has been reported that the resulting surface roughness on brittle materials is related to SSD, as shown in Eq. (1) [15]:

$$\frac{SSD}{SR} = 2.33\alpha_k \left(\frac{E}{H} \right)^{\frac{2-5m}{3}} \frac{(\cot \psi)^9}{(\sin \psi)^2} \left[\frac{P}{K_C^4 / H^3} \right]^{\frac{1}{6}} \quad (1)$$

where E, H, and Kc are the material's Young's modulus, hardness, and fracture toughness, respectively; ψ is the abrasive included angle; P is the indenting force on the abrasive; α_k and m are coefficients.

Similarly, the correlation between SSD depth and processing parameters is reported to serve as empirical rule-of-thumb to estimate the upper and lower bond of SSD depth. For example, a model by Lambropoulos [16] predicts SSD depth range for surfaces processed by deterministic microgrinding, lapping, and sawing and another by Suratwala [17] for fixed-abrasive ground, loose-abrasive ground, and sanded surfaces are shown in Fig. 3.

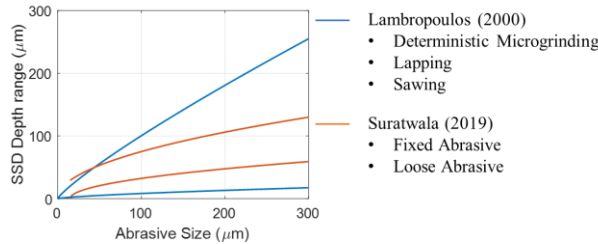


Fig. 3. Non-destructive predictive models for SSD depth upper and lower bound determination from abrasive size for various processing methods.

We herein present a destructive method that combines multiple material characterization techniques to track evolution of material characteristics with penetration depth into the tested surface and thus extract SSD. By focusing on more than surface roughness and morphologies

of damaged material, we aim to assess SSD not only in the form of cracks but also other possible damage types, such as residual stresses and material melting. First, our work fills the area where tested surfaces are with sub-micron surface roughness; second, we assessed SSD induced by both deterministic microgrinding and ultrafast laser processing, and thus their similarities and differences are shown.

2. Materials and Methods

2.1 Materials

For substrates, we chose three types of commonly used optical glass: N-BK7, Borofloat 33 (BF33), and Fused Silica (FS).

We used three pieces of cylindrical (24 mm in diameter, 6 mm in thickness) N-BK7 substrates, three pieces of FS substrates with the same geometry and dimension as N-BK7 substrates, and one piece of cuboid (1mm W * 1mm L * 1.75 mm T) BF33 substrates. Material properties are listed in Table 1.

Table 1. Mechanical and optical properties of materials at 25°C [18] [19] [20].

Material	Density, g/cm ³	Young's Modulus, GPa	Knoop Hardness, HK 0.1/20, GPa	Refractive Index n _d	Coefficient of Thermal Expansion, K ⁻¹
N-BK7	2.51	82	6.0	1.516	7.10E-06
Borofloat 33	2.23	63	4.8	1.471	3.30E-06
Fused Silica	2.20	72	5.1	1.458	5.50E-06

2.2 Sample preparation

1. Deterministic micro-grinding

Deterministic microgrinding platforms grind components with rigid, computer-controlled machining centers and high-speed tool spindles. We used OptiPro eSX 50 CNC machine with a series of several z-plunge processed in the setup shown in Fig. 4 (a) [21] using diamond ring tools with 2 – 4 μm diamond abrasives (Fig. 4 (b)) to introduce SSD to FS and N-BK7 surfaces. Material removal of each grinding process is large enough to remove damages caused by previous processing. Surfaces are accepted if surface roughness peak-to-valley (PV) is less than 1μm for BK7 and less than 0.5 μm for FS. Morphologies of typically accepted surfaces are shown in Fig. 5.

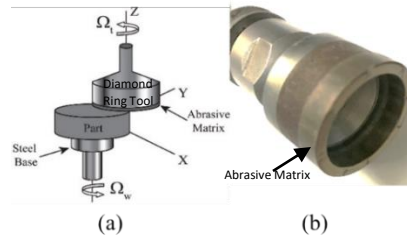


Fig. 4. Schematics of the ring tool grinding configuration used in our experiments (a) [21] and metal bronze bonded diamond ring tool with 2-4 μm diamond grit (b). Diamond abrasives are embedded in abrasive matrix. Subfigure (a) adapted with permission from S. Shafir et al. (2007).

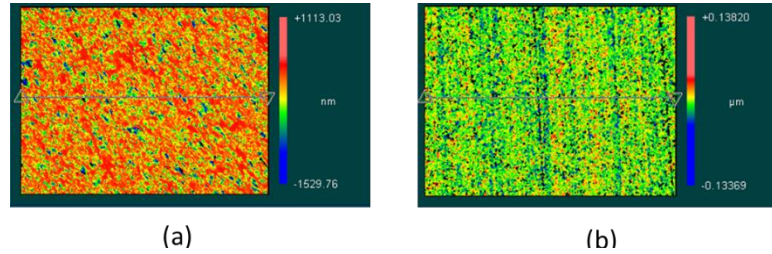


Fig. 5. Morphologies of typical accepted (a) N-BK7 surface and (b) FS surface measured by Zygo NewView interferometer.

2. Femtosecond laser processing

Femtosecond laser polishing has the potential to overcome limitations of CO₂ laser polishing, such as limited material compatibility, large surface profile errors, and surface roughness of processed surfaces. Like CO₂ laser polishing, femtosecond laser polishing is also efficient and predictable. However, it can be applied to a wider range of materials and can achieve better surface quality when properly operated [22].

In this study, borofloat samples were processed using femtosecond laser [23]. With optimized parameters, the setup can remove visible cosmetics (Fig. 6). Typical laser-processed zones are squares of 100 μm by 100 μm, and the amount of material removed varied depending on number of area laser passes and energy density, ranging from 5 to 40 nm. The surface roughness of processed area varied from 0.61 to 0.68 nm RMS.

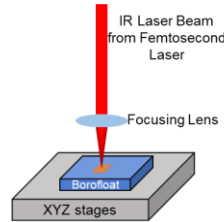


Fig. 6. Illustration of experimental setup used for femtosecond laser processing.

2.3 Methods

The flowchart of SSD assessment methods is shown in Fig. 7.

For ground N-BK7 and FS surfaces that are large enough to accommodate MRF spots, we firstly put MRF spot of different depths on the tested surfaces and measure the average material removal rate and surface roughness at deepest part penetration at each spot to reveal material damage.

After that, for normal (i.e., non-densifying) glass material that initiates radial cracks with micro-indentations (e.g., N-BK7), we put Vicker's micro indentations inside the MRF spots and measure the fracture toughness based on indentation crack sizes. SSD will be assessed by evolution of fracture toughness with spot depths; while for anomalous (i.e., densifying and thus not able to produce radial cracks) glass material (e.g., FS), we put eight nanoindentation arrays containing one by thirty nanoindentations in the MRF spots and extract Young's modulus and hardness to visualize SSD.

For laser-processed area on borofloat substrates, since they are too small to accommodate MRF spots, we put nanoindentation arrays directly on the tested surface. Nanoindentation arrays are very sensitive to material damage even at small (tens of nanometers) depth.

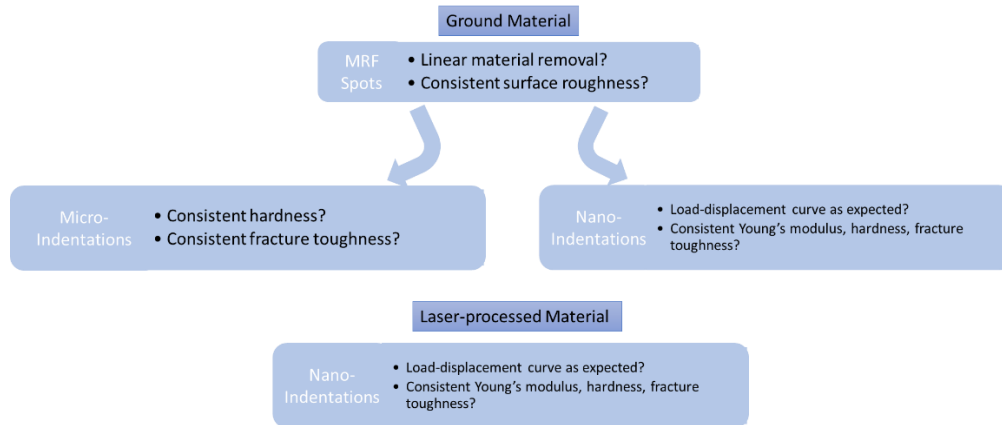


Fig. 7. Flowchart of SSD assessment methods

1. MRF spotting

We produce MRF spots in different depths by changing the dwell time when MR fluid is in contact with the tested surface. For each dwell time, we create a set of 4 MRF spots. Figure 8 (a) shows a BK7 tested surface with 2 sets of MRF spots measured by OptiPro UltraSurf. Fig. 8 (b) is the trace profile of one of the MRF spots. Spot depth is recorded as the deepest part penetration (DDP).

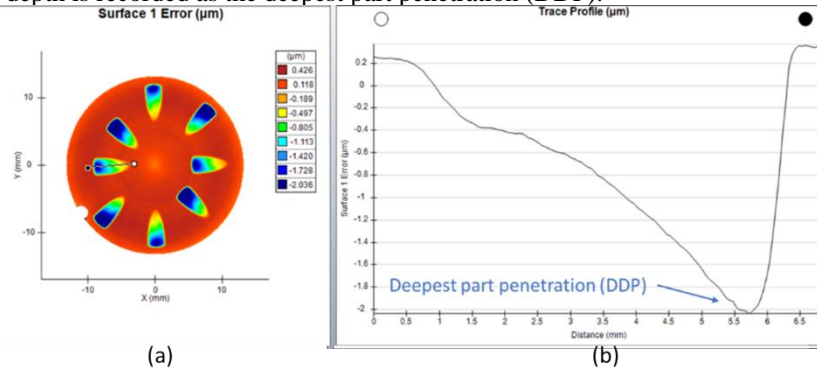


Fig. 8. (a) Ground BK7 surface with 2 sets of MRF spots and (b) the trace profile of one of the spots. The spot shown in (b) was spotted with duration time of 40s. Peak-to-valley (PV) of the right plot was recorded as spot depth of the corresponding spot.

2. Vicker's micro-indentation

Vickers' hardness micro-indenters were put both on ground surface and at DDP of each MRF spot, to extract fracture toughness (K_C) and residual stress (σ). Three loads were used for micro-indentations: 100g, 200g and 500g. We put 12 indents on each ground surface with 4 for each load, and 3 indents at DDP of each spot, 1 for each load.

Based on dimensions of the micro-indentations and radial cracks, we extract fracture toughness (K_C) of the material using Eq. (2) [24], where E , H , and K_C stand for Young's modulus, hardness and fracture toughness of the indented material, respectively; C is half crack length associated with the micro indentation, and D is diagonal of micro indentation. Through Vicker's indentations inside MRF spots of different depths, we observe how K_C evolves with depth and therefore determine material damage level at each depth.

$$K_C = H \sqrt{\frac{D}{2}} \left(\frac{E}{H} \right)^{0.4} 10^{f(x)}$$

$$x = \log_{10} \left(\frac{C}{D/2} \right)$$

$$f(x) = -1.59 - 0.34x - 2.02x^2 + 11.23x^3 - 24.97x^4 + 16.32x^5 \quad (2)$$

3. Nanoindentation array tests

Nanoindentation determines hardness and Young's modulus of a material through load-displacement behavior of the material tested with a Berkovich indenter. Hardness and Young's modulus are extracted using Oliver & Pharr method using Eq. (3) [25]:

$$S = \frac{dP}{dh} = \frac{2\beta}{\sqrt{\pi}} E_r \sqrt{A}$$

$$\frac{1}{E_r} = \frac{1-\nu^2}{E} + \frac{1-\nu_i^2}{E_i}$$

$$H = \frac{P_{\max}}{A} \quad (3)$$

where P and h stand for load and displacement of indenter tip, respectively, A the projected area of indenter tip at indented surface, E Young's modulus, ν Poisson's ratio, and H hardness. β is a geometrical constant on the order of unity. The subscript i denotes for indenter, r reduced, and max the maximum.

For ground FS material, we created a 3 by 3 nanoindentation array at DDP of each MRF spots, and another 3 by 3 nanoindentation array at each ground surface.

For laser processed BF33 material, we used several 1 by 30 nanoindentation arrays to cover all the laser-processed area from edge to center (Fig. 9). The horizontal spacing between neighboring indentations is 20 μm . Vertical spacing between neighboring arrays is 40 μm .

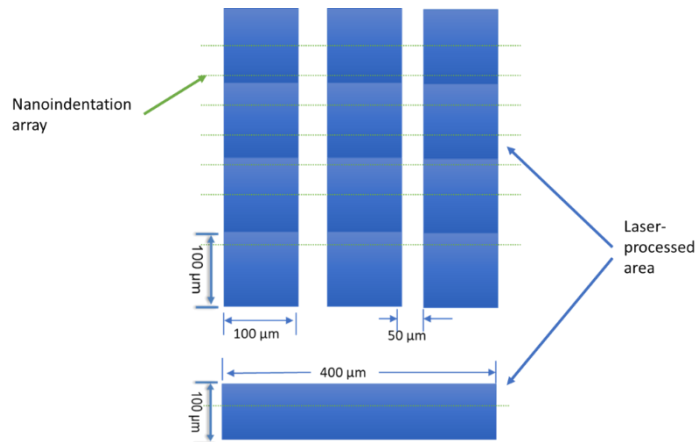


Fig. 9. Nanoindentation array design on laser-processed material. The blue boxes represent laser-processed spots, with peak laser influence 1.77 – 2.34 J/cm², number of passes 20 – 60, laser speed 0.8 – 1.0 mm/s. The dashed lines represent nanoindentation arrays, each of 1 by 30 nanoindentations spaced by 20 μm .

3. Results

3.1 MRF spotting

Figure 10 [26] shows results of MRF spotting in material removal rate (MRR) and surface roughness PV. Each data point represents results from all the MRF spots with the same duration time that MR fluid is in contact with the tested surface, with its horizontal coordinate being the average depth of these spots. The MRF spots varied in depths to 1.5 μm for FS, and to 3.5 μm for N-BK7. The number of different spots and measurements per spot are given in section 2.3.

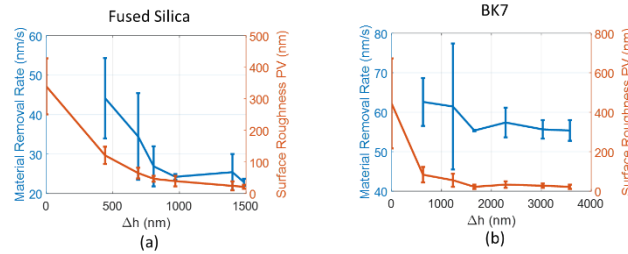


Fig. 10. Material removal rate (MRR) of MRF spots and surface roughness PV at deepest depth penetration (DDP) of the corresponding spot on (a) fused silica and (b) N-BK7. Figure adapted with permission from J. Xu et al. (2019) [26].

3.2 Vicker's micro-indentations

Figure 11 [26] shows fracture toughness K_C extracted from Vicker's micro-indentations on N-BK7 substrates using Eq. (2). The depths of the spots within which the indentations were placed varied from 500 nm to 3500 nm. The number of different spots and different indentations per spot are given in section 2.3.

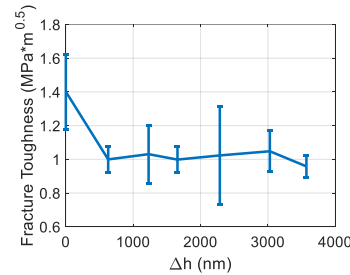


Fig. 11. Plot of fracture toughness on ground surfaces and at DDP of each MRF spot. Each data point represents the average of all the spots with the same duration time. Figure adapted with permission from J. Xu et al. (2019) [26].

3.3 Nanoindentation array tests

Figure 12 shows Young's modulus extracted from nanoindentation array test results on ground FS surface and inside DDP of MRF spots, together with Young's modulus of pristine FS material from datasheet [20]. For ground surface, the plot shows the average of the nanoindentation array test results from all the ground FS surface; for MRF spots, each plot shows the average of nanoindentation array test results within all the MRF spots with the same duration time that MR fluid is in contact with the tested surface.

Figure 13 shows part of four nanoindentation arrays on laser-processed spots. For each array, eight indentations can be seen here. Overall, we have 19 accepted indentations on unprocessed material and 80 accepted indentations on laser-processed material.

Figure 14 shows Young's modulus of laser-processed BF33 material and pristine BF33 material extracted from nanoindentation array tests shown in Fig. 13, compared with Young's modulus of pristine BF33 from datasheet [27].

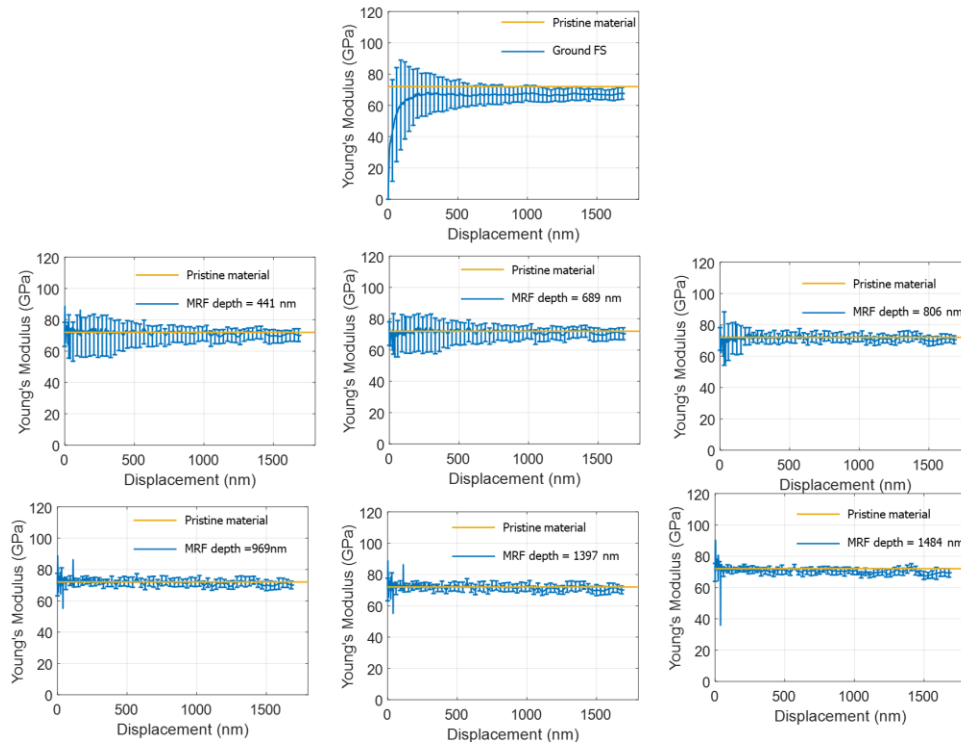


Fig. 12. Young's modulus extracted from nanoindentation array tests on ground FS and inside deepest depth penetration of MRF spots of different depths. For MRF data, the plots are arranged in order of increasing depths of MRF spots.



Fig. 13. Nanoindentation arrays on laser-processed spots, measured by Keyence microscope.

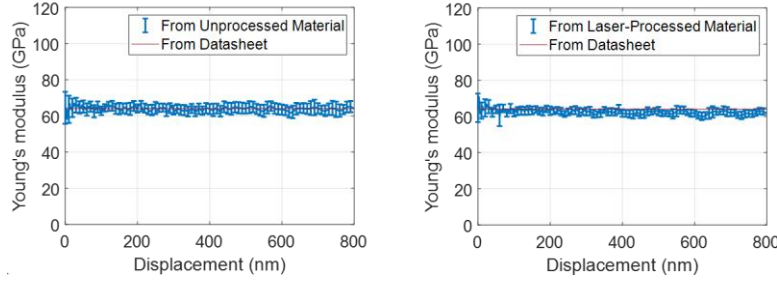


Fig. 14. Plots of Young's modulus evolution with depth measured by nanoindentation arrays compared with Young's modulus value from vendor's datasheet.

4. Discussion

4.1 MRF Spotting

According to Fig. 10, for both FS and N-BK7, surface microroughness peak-to-valley (PV) and material removal rate (MRR) level off as spots penetrate more deeply since initial surface roughness and cracks in SSD are being removed. When the spot penetrates beyond SSD layer, the plot flattens out because the spot has reached undamaged material and in-spot microroughness is no longer affected by damage extent.

SSD depths estimated by Fig. 10 are $0.80\ \mu\text{m} - 0.97\ \mu\text{m}$ for FS and $0.63\ \mu\text{m} - 1.67\ \mu\text{m}$ for N-BK7.

4.2 Vicker's micro-indentations

According to Fig. 11, for N-BK7 fracture toughness shows the same evolution trend as SR and MMR, and the depth-independent part matches pristine value as listed in Table 1. According to the points where fracture toughness becomes constant, SSD depth estimated from fracture toughness is $0.63\text{-}1.23\ \mu\text{m}$ for N-BK7.

The decrease of fracture toughness within SSD depth also reveals the release of compressive residual stress caused by material damage. Change of fracture toughness from pristine value has a positive correlation with residual stress [28]:

$$\Delta K_c = \frac{1.04\sigma\sqrt{\pi(2c)}}{\sqrt{2.64}} \quad (4)$$

where σ is compressive stress on ground surface, and c is the half length of the radial crack induced by Vickers' indentation.

According to Eq. (4), residual stress at the top of tested ground N-BK7 surface can be estimated as $31\pm 5\ \text{MPa}$.

4.3 Nanoindentation array tests

1. Ground FS surface

As can be seen from Fig. 15, for ground FS surface and inside shallow (depth < SSD depth estimated in section 4.1) MRF spots, Young's modulus extracted from nanoindentation array test results starts low with larger standard deviations for damaged material, and then converges to pristine value with smaller standard deviations when the indenter tip reaches undamaged material. For deep (depth > SSD depth estimated in section 4.1) MRF spots, the indenter tip only penetrates undamaged material. The corresponding Young's modulus stays constant at pristine value with small deviations.

We observed that nanoindentation response of undamaged FS material is identical to that in MRF spots of depth greater than SSD. We used this feature to determine SSD depth by calculating power of the nanoindentation array test at each indenter tip penetration

displacement, which is the probability that Young's modulus extracted from nanoindentation response of undamaged FS and of to-be-compared FS material are the same at the corresponding indenter tip displacement.

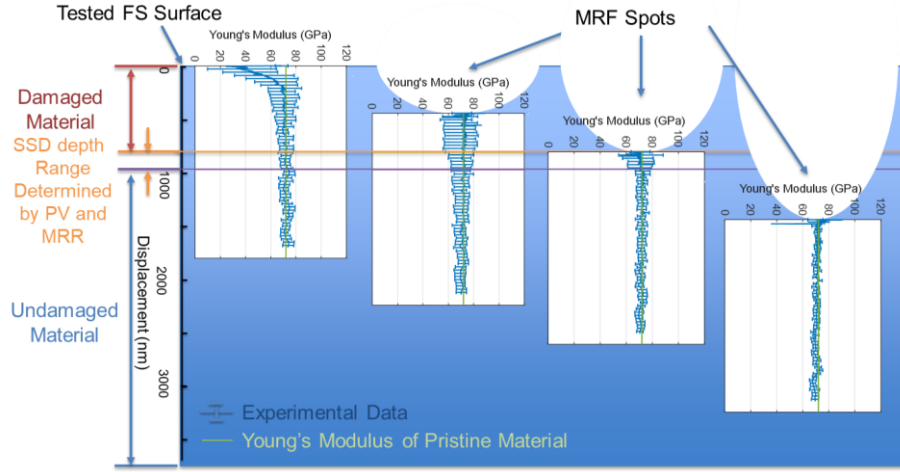


Fig. 15. Nanoindentation responses of damaged and undamaged FS.

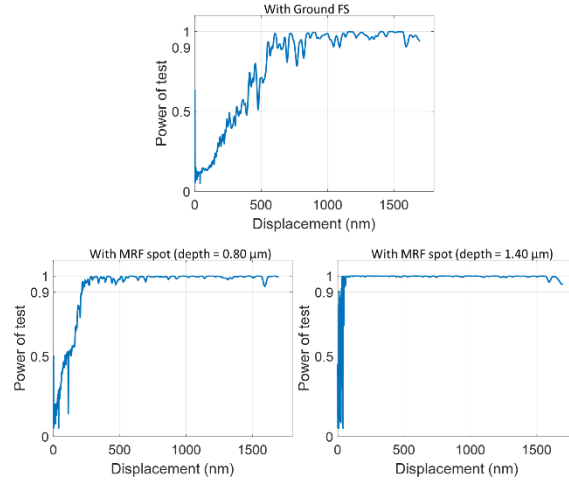


Fig. 16. Power of test that ground FS response, shallow (depth < SSD estimated in section 4.1) MRF spot response, and large (depth > SSD estimated in section 4.1) MRF spot response are the same as undamaged FS response.

We used results from nanoindentation arrays inside MRF spots of $1.48 \mu\text{m}$ as nanoindentation response of undamaged FS and used those from all other arrays as to-be-compared nanoindentation responses. At each depth, we calculated power of test that these two responses are the same. A high power of test value (close to 1) means the compared nanoindentation response is the same, suggesting no subsurface damage at the corresponding depth and material.

Fig. 16 plots power of test that ground FS response, shallow (depth < SSD estimated in section 4.1) MRF spot response, and large (depth > SSD estimated in section 4.1) MRF spot response are the same as undamaged FS response. Power of test always converges to 1 as nanoindenter tip approaches the undamaged material.

Table 2 lists SSD depth extracted from power of tests that each of the to-be-compared responses are the same as undamaged FS response. The end of damaged material was determined as the last point where power of test is lower than 0.9. SSD depth was determined by adding MRF depth and end of damaged material.

By averaging from Table 2, SSD depth of ground FS surface estimated by nanoindentation array test results is $1.20 \mu\text{m} \pm 0.26 \mu\text{m}$.

Table 2. SSD depth extracted from power of tests. The estimated SSD depth is found by adding the MRF spot depth and the end of damaged material as determined by nanoindentation.

MRF spot depth (nm)	End of damaged material (nm)	Estimated SSD depth (nm)
0	830	830
441	940	1381
689	760	1449
806	213	1019
969	116	1085
1397	47	1444

2. Laser-processed BF33 surface

We separated nanoindentation array test results of pristine (unprocessed) BF 33 into two groups, and calculated power of test that these two responses are the same. Then we calculated power of test that nanoindentation response of laser processed and unprocessed BF 33 (Fig. 13) are the same. Results are plotted in Fig. 17.

For pristine vs pristine material, power of test stays larger than 0.9 starting from 55 nm, suggesting that nanoindentation array test can test SSD of over 55 nm with over 90% confidence on BF 33.

For pristine vs laser-processed material, power of test stays larger than 0.9 for indenter tip displacement over 55 nm, suggesting no detectable SSD of over 55 nm on tested laser-processed material.

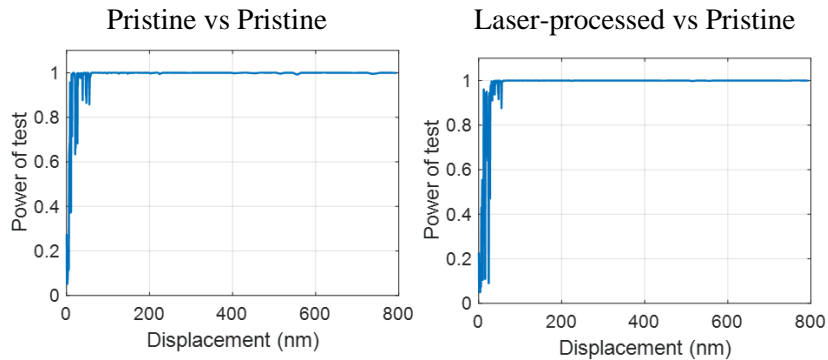


Fig. 17. Power of test calculated based on comparison of nanoindentation responses of pristine VS pristine BF 33 (left) and laser-processed VS pristine BF 33 (right).

4.4 Comparison

A comparison of all the protocols used for each material with corresponding material properties is shown in Table 3. No detectable SSD of over 55 nm was assessed on laser-processed BF 33. For each ground surface, SSD estimated by two different protocols agree with each other.

We must emphasize that our observation of not detectable SSD of depth greater than 55 nm does not imply that there is damage below 55 nm. Power of nanoindentation array tests indicates that results from the nanoindentation method was indistinguishable between the pristine and laser processed material when the indenter tip penetration displacement is less than 55 nm. Our goal in this report is to assess sub-micrometer damage by using nanoindentation.

Table 3. All SSD assessment protocols used for each material and their results.

Tested surface	Protocol	Estimated SSD (μm)	Average SSD depth (μm)	$E^{1/2}/H$ ($\text{GPa}^{-1/2}$)
Ground N-BK7	MRF spotting	0.63 - 1.67		
	Vicker's micro-indentation	0.63 - 1.23	1.04	1.51
Ground FS	MRF spotting	0.80 - 0.97		
	Nanoindentation array tests	1.20 ± 0.26	1.04	1.65
Laser-processed BF 33	Nanoindentation array tests	No detectable SSD of over 55 nm		

According to Table 3, SSD depths of ground N-BK7 and FS are similar. This result is expected since both materials were subjected to the same grinding process, and both have similar material properties. Previous study has shown that SSD depth is correlated to material properties as $E^{1/2}/H$ where E is the Young's modulus, H is the hardness of the material [17]. This value is very similar for N-BK7 and for FS, leading to similar SSD depth of both materials for the same grinding process.

Table 3 also shows relatively small variations of estimated SSD. This can be attributed to sensitivity of material properties to material damage level. Material properties such as fracture toughness, Young's modulus and hardness are very sensitive to material damage level, and these properties can be measured at different penetration depths by varying deepest depth penetration (DDP) of MRF spots and using nanoindentation. Therefore, combining microscopic observation of damaged material exposed by MRF spots and tracking of material properties as a function of penetration depth, with sufficient repeatability, can assess SSD depth more precisely than wedging methods that involves microscopic observation only.

When compared with previous studies [10,29,5,8], the present work here was able to refine the near-surface region where surface roughness and SSD depths are sub-micron level (Fig. 18). We showed that low surface roughness (0.4 - 0.5 μm peak-to-valley) does not necessarily lead to absolute absence of SSD. In addition, our metrology is effective for not only cracks, but also all other damage types that change mechanical properties, which allows our metrology to test substrates from mechanically processed (fixed abrasive ground, loose abrasive ground or polished, and lapped) to laser processed.

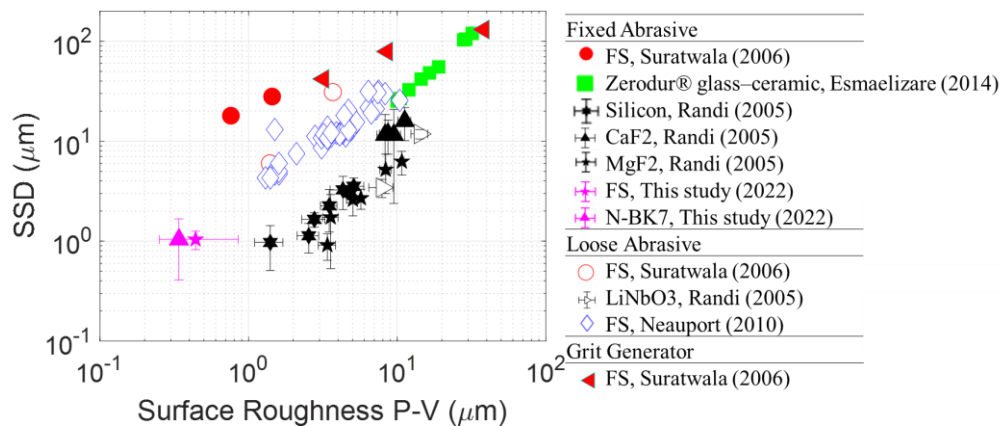


Fig. 18. Comparison of the measured vs surface roughness P-V of ground FS.

5. Conclusions

An effective SSD assessment metrology based on tracing of material characteristics including fracture toughness, behavior under micro- and nano-indentations, and material removal and roughness with MRF spots has been demonstrated for optical glass surfaces processed by deterministic microgrinding and ultrafast laser processing. This metrology precisely measures SSD depth with high confidence and is preferred when surface roughness and expected SSD depth are sub-micron level and up. This metrology is shown to be effective for damages induced by mechanical processing and is used to demonstrate the absence of damage in ultrafast laser-processed optical surfaces.

Funding

This research was supported by the National Science Foundation I/UCRC Center for Freeform Optics (IIP-1338877 and IIP-1338898.)

Disclosures

The authors declare no conflicts of interest.

Data Availability

Data underlying the results presented in this paper are not publicly available at this time but may be obtained from the authors upon reasonable request.

References

- [1] D. Korytar, Z. Zaprazny, C. Ferrari, C. Frigeri, M. Jergel, I. Matko, and J. Keckes, "Cross-sectional TEM study of subsurface damage in SPDT machining of germanium optics," *Appl. Opt.* **58**(8), 1940-1943 (2018).
- [2] J. Lambropoulos, S. Xu, T. Fang, and D. Golini, "Twyman effect mechanics in grinding and microgrinding," *Appl. Opt.* **35**(28), 5704-5713 (1996).
- [3] E. N. Pugh, and L. E. Samuels, "Damaged layers in abraded silicon surfaces," *J. Electrochem. Soc.* **111**(12), 1429 (1964).
- [4] S. N. Shafrir, J. C. Lambropoulos, and S. D. Jacobs, "Subsurface damage and

mcirostructure development in precision microground hard ceramics using magnetorheological finishing spots," *Appl. Opt.* **46**(22), 5500 (2007).

- [5] J. Neauport, "Loose abrasive slurries ofr optical glass lapping," *Appl. Opt.* **49**(30), 5736-5745 (2010).
- [6] T. O. Mulhearn, "The deformation of metals by Vickers-type pyramidal indenters," *J. Mech. Phys. Solids* **7**, 85-96 (1959).
- [7] H. Wang, C. Wang, J. Liu, S. Gao, and W. Zhai, "Analysis of surface and subsurface damage morphology in rotary ultrasonic machining of BK7 glass," *IOP Conf. Ser.: Mater. Sci. Eng* **269** 012071 (2017).
- [8] A. Esmaeilzare, A. Rahimi, and S. Rezaei, "Investigation of subsurface damage and surface roughness in grinding process of Zerodur glass-ceramic," *Appl. Surf. Sci.* **313**, 67-75 (2014).
- [9] J. Randi, J. Lambropoulos, and S. Jacobs, "Subsurface damage in some single crystalline optical materials," *Appl. Opt.* **44**(12), 2241-2249 (2005).
- [10] T. Suratwala, L. Wong, P. Miller, M. Feit, J. Menapace, R. Steele, P. Davis, and D. Walmer, "Sub-surface mechanical damage distributions during grinding of fused silica," *Journal of Non-Crystalline Solids* **352**, 5601-5617 (2006).
- [11] C. Miao, K. Bristol, A. Marino, S. N. Shafrir, J. E. Degroote, and S. D. Jacobs, "Magnetorheological fluid telate for basic studies of mechanical-chemical effects during polishing," *Proc. SPIE* **6671**, 667110 (2007).
- [12] J. DeGroote, H. Romanofsky, Irina Kozhinova, John Schoen, and Stephen Jacobs, "Polishing PMMA and other optical polymers with magnetorheological finishing," *Proc. SPIE* **5180**, 123 - 134(2003).
- [13] J. Jang, M. J. Lance, S. Wen, and G. M. Pharr, "Evidence for nanoindentation-induced phase transformations in germanium," *Appl. Phys. Lett.* **86**, 131907 (2005).
- [14] U. Bismayer, J Chrosch, and E. Salje, "Anti-phase boundaries and phase transitions in titanite: An X-ray diffraction study," *American Mineralogist* **82**, 677-681 (1997).
- [15] J. C. Lambropoulos, S. D. Jacobs, and J. Ruckman, "Material removal mechanisms from grinding to polishing," *Cream. Trans.* **102**, 113-128 (1999).
- [16] J. C. Lambropoulos, "FROM ABRASIVE SIZE TO SUBSURFACE DAMAGE IN GRINDING," in *Optical Fabrication and Testing* (2000), paper OMA6.

- [17] T. Suratwala, W. Steele, L. Wong, G. Tham, J. Destino, P. Miller, N. Ray, J. Menapace, E. Feigenbaum, N. Shen, and M. Feit, "Subsurface mechanical damage correlations after grinding of various optical materials," *Opti. Eng.* **58**(9), 092604 (2019).
- [18] SCHOTT, "Borofloat 33 - Mechanical Properties," (2022)
<https://www.schott.com/en-us/products/borofloat-p1000314/downloads>.
- [19] SCHOTT, "SCHOTT N-BK7," (2014)
<https://www.schott.com/shop/medias/schott-datasheet-n-bk7-eng.pdf?context=bWFzdGVyfHJvb3R8NjkxODAwfGFwcGxpY2F0aW9uL3BkZnxoZTUvaDM4Lzg4MTAzMTYxMDM3MTAucGRmfGJjNmI4ZjFmY2Q1NjMxMTE0MjkzMTUwOGRmMTUzOTg2NWJjZTgzMjA0OTc2NTNiMThjN2RhMjI4NGZmMWM4MWU>.
- [20] H. Bach and N. Neuroth, *The properties of optical glass*, (Springer, 1995).
- [21] S. Shafir, J. Lambropoulos and S. Jacobs, "MRF spotting technique for studying subsurface damage in deterministic microground polycrystalline alumina," *Proc. SPIE* **6671**, 66710J (2003)
- [22] L. L. Taylor and J. Qiao, "Optimization of femtosecond laser processing of silicon via numerical modeling," *Opti. Mater. Express* **6**, 2745-2758 (2016).
- [23] G. Chen and J. Qiao, "Femtosecond-laser-enabled simultaneous figuring and finishing of glass with a subnanometer optical surface," *Opti. Lett.* **47**(15), 3860 (2022).
- [24] J. C. Lambropoulos, T. Fang, P. D. Funkenbusch, S. D. Jacobs, M. J. Cumbo, and D. Golini, "Surface microroughness of optical glasses under deterministic microgrinding," *Appl. Opt.* **35**(22), 4448-4462 (1996).
- [25] W. C. Oliver and G. M. Pharr, "An improved technique for determining hardness and elastic modulus using load and displacement sensing indentation experiments," *J. Mater. Res.* **7**(6), 1564-1583 (1992).
- [26] J. Xu, L. Taylor, J. Qiao, M. Pomerantz, and J. Lambropoulos, "Subsurface damage measurement of single crystal germanium and borosilicate glass BK-7," *Proc. SPIE* **11175**, 1117508 (2019)
- [27] SCHOTT, "SCHOTT optical glass data sheets," SCHOTT (2019)
https://www.schott.com/d/advanced_optics/ac85c64c-60a0-4113-a9df-23ee1be20428/1.14/schott-optical-glass-collection-datasheets-english-may-2019.pdf.

- [28] Y. Murakami, *Stress intensity factors handbook*, (Pergamon, 1987).
- [29] J. A. Randi, J. C. Lambropoulos, and S. D. Jacobs, "Surface damage in some single crystalline optical materials," *Appl. Opt.* **44**(12), 2241-2249 (2005).
- [30] Y. Li, "Morphology and distribution of subsurface damage in optical fused silica parts: bond-abrasive grinding," *Appl. Surf. Sci.* **257**(6), 2066-2073 (2011).
- [31] Z. Dong and H. Cheng, "Study on removal mechanism and removal characters for SiC and fused silica by fixed abrasive diamond pellets," *Int. J. Mach. Tools Manuf.* **85**, 1-13 (2014).
- [32] D. Lv, "Subsurface damage depth and distribution in rotary ultrasonic machining and conventional grinding of glass BK7," *Int. J. Adv. Manuf. Technol.* **86**, 2361-2371 (2016).
- [33] Z. Wang, "Subsurface damage distribution in the lapping process," *Appl. Opt.* **47**(10), 5736-5745 (2008).
- [34] E. Pugh and L. Samuels, "Damaged layers in abraded silicon surfaces," *J. Electrochem. Soc.* **111**(12), 1429-1431 (1964).